

Implications of ice-shelf hydrofracturing and ice-cliff collapse mechanisms for sea-level projections

Robert E. Kopp¹, Robert M. DeConto², Daniel A. Bader³, Carling C. Hay^{1,4}, Radley M. Horton³, Scott Kulp⁵, Michael Oppenheimer⁶, David Pollard⁷, Benjamin H. Strauss⁵

¹Department of Earth & Planetary Sciences and Institute of Earth, Ocean & Atmospheric Sciences, Rutgers University,
New Brunswick, NJ, USA

²Department of Geosciences, University of Massachusetts–Amherst, Amherst, MA, USA

³Center for Climate Systems Research, Columbia University, New York, NY, USA

⁴Department of Earth & Planetary Sciences, Harvard University, Cambridge, MA, USA

⁵Climate Central, Princeton, NJ, USA

⁶Woodrow Wilson School of Public & International Affairs and Department of Geosciences, Princeton University,

Princeton, NJ, USA

⁷Earth and Environmental Systems Institute, Pennsylvania State University, University Park, PA, USA

Key Points:

- Ice-shelf hydrofracturing and ice-cliff collapse mechanisms significantly revise high-emissions sea-level projections upwards.
- Late-21st century sea level is more heavily emissions-dependent than indicated by most prior projections.
- Current Antarctic mass loss is driven by different processes than and exhibits little correlation with late-century changes.

Abstract

Probabilistic sea-level projections have not yet integrated insights from physical ice-sheet models representing mechanisms, such as ice-shelf hydrofracturing and ice-cliff collapse, that can rapidly increase ice-sheet discharge. Here, we link a probabilistic framework for sea-level projections to a small ensemble of Antarctic ice-sheet (AIS) simulations incorporating these physical processes to explore their influence on projections of global-mean sea-level (GMSL) and relative sea-level (RSL) change. Under high greenhouse gas emissions (Representative Concentration Pathway [RCP] 8.5), these physical processes increase median projected 21st century GMSL rise from ~80 cm to ~150 cm. Revised median RSL projections would, without protective measures, by 2100 submerge land currently home to > 79 million people, an increase of ~25 million people. The use of a physical model, rather than simple parameterizations assuming constant acceleration, increases sensitivity to forcing: overlap between the central 90% of the frequency distributions for 2100 for RCP 8.5 (93–243 cm) and RCP 2.6 (26–98 cm) is minimal. By 2300, the gap between median GMSL estimates for RCP 8.5 and RCP 2.6 reaches > 10 m, with median RSL projections for RCP 8.5 jeopardizing land now occupied by ~900 million people (vs. ~80 million for RCP 2.6). There is little correlation between the contribution of AIS to GMSL by 2050 and that in 2100 and beyond, so current sea-level observations cannot exclude future extreme outcomes. These initial explorations indicate the value and challenges of developing truly probabilistic sea-level rise projections incorporating complex ice-sheet physics.

1 Introduction

Over the last several years, multiple authors have generated estimates of partial or full probability distributions of future global-mean sea level (GMSL) and local relative sea-level (RSL) changes, conditional upon greenhouse gas emissions scenarios [e.g., *Kopp et al.*, 2014, 2016; *Mengel et al.*, 2016; *Slangen et al.*, 2014; *Jackson and Jevrejeva*, 2016]. There is a good degree of agreement among many of the studies, as well as between these studies and the IPCC's Fifth Assessment Report [AR5: *Church et al.*, 2013a]. In some cases, this is by construction (e.g., the agreement between AR5 and *Kopp et al.* [2014]). In other cases, this agreement represents independent lines of evidence leading to similar conclusions: for example, the agreement between AR5 and recent semi-empirical models relating GMSL change to global-mean temperature [*Kopp et al.*, 2016; *Mengel et al.*, 2016].

This agreement is not universal, however [e.g., *Jackson and Jevrejeva*, 2016], and may be misleading. The response of polar ice sheets to forcing remains an area of deep uncertainty [*Kasperson*, 2008; *Heal and Millner*, 2014], and additional approaches beyond historically calibrated statistical models [*Kopp et al.*, 2016; *Mengel et al.*, 2016] and consensus-based expert assessment [*Church et al.*, 2013a] can also provide reasonable ways of estimating the probability distribution of the ice-sheet response. Notably, structured expert elicitation about the Antarctic ice sheet (AIS) response [*Bamber and Aspinall*, 2013] yielded a broader range than consensus-based AR5 expert assessment. Direct use of results from this expert-elicitation study drives the higher projections in *Jackson and Jevrejeva* [2016]. Moreover, while most process models of the AIS response have been consistent with AR5, *DeConto and Pollard* (*DeConto and Pollard* [2016]; henceforth, DP16) found that the inclusion of previously omitted physical processes such as ice-shelf hydrofracturing and structural collapse of tall, marine-terminating ice cliffs has the potential to drive an order-of-magnitude increase in Antarctic mass-loss rates.

Ideally, the integration of process models into probabilistic frameworks such as those of *Kopp et al.* (*Kopp et al.* [2014]; henceforth, K14) and *Jackson and Jevrejeva* [2016] would involve the development and use of fast models – or fast statistical emulators of more complex models – in a mode that allows Monte Carlo sampling of key uncertainties and the conditioning of uncertain parameters on multiple observational lines of evidence. The development of such fast models or model emulators is an involved task, however, and the publica-

tion of DP16 triggered an increase in stakeholder interest and a demand for more *ad hoc* approaches. For example, regional sea-level assessments for the City of Boston [Douglas *et al.*, 2016] and State of California [Cayan *et al.*, 2016] adopted the K14 framework but substituted, as a set of discrete samples, an ensemble of Antarctic ice-sheet projections from DP16. The U.S. Global Change Research Program’s Climate Science Special Report [Wuebbles *et al.*, in review] and a U.S. Interagency Task Force on Sea-Level Rise report [Sweet *et al.*, 2017] more qualitatively assessed how DP16’s results might shift the probability distribution of future GMSL change.

Here, we extend the approach of Douglas *et al.* [2016] and Cayan *et al.* [2016] to a global scale, substituting DP16’s Antarctic ice sheet ensembles for K14’s expert assessment- and expert elicitation-based probability distribution. The resulting GMSL and RSL projections should not be viewed as probabilistic; the DP16 ensembles were not constructed from coherent, probabilistic prior distributions of key parameters, and are conditioned only on a very limited set of observational constraints, taken from paleo-sea level reconstructions. Accordingly, we refer to the resulting distributions as *frequency distributions*, not *probability distributions*. Rather than providing quantitatively revised probability distributions of future sea-level change, the DP16 frequency distributions should be viewed as providing semi-quantitative information about potential future changes and the degree of deep uncertainty in sea-level projections. This deep uncertainty highlights the weight that should be given to high-consequence, low-likelihood tail projections in risk management (e.g., protection of long-lifetime critical infrastructure), as well as the need for adaptive management strategies, and emphasizes that, at present, no sea-level rise projections can provide unique, ‘true’ probability estimates. We also use these projections to explore the limitations arising in past probabilistic approaches from reliance upon expert elicitation of melt rates at a single time point and the assumption of linear changes in melt rates.

2 Methods

2.1 Projections Framework

The framework employed to generate probabilistic GMSL and RSL projections in this analysis is based on that of K14. The K14 framework combines multiple lines of information to construct probability distributions for key contributors to GMSL and RSL change. It employs a joint probability distribution for global mean thermal expansion and regional ocean dynamics derived from the Coupled Model Intercomparison Project Phase 5 (CMIP5) [Taylor *et al.*, 2012] ensemble. Its projections of glacier mass-balance changes are derived from the Marzeion *et al.* [2012] surface mass-balance model, forced by the CMIP5 ensemble. Following the approach of Rahmstorf *et al.* [2012], its projections of the global-mean contribution of anthropogenic changes in land-water storage are based upon historical relationships between human population, dam construction, and groundwater withdrawal [Chao *et al.*, 2008; Wada *et al.*, 2012; Konikow, 2011]. The regional contributions of non-climatic effects such as glacio-isostatic adjustment, tectonics, and sediment compaction are based upon a spatiotemporal statistical model of tide-gauge observations. Ice sheet contributions are derived from the AR5 expert assessment and the structured expert elicitation of Bamber and Aspinall [2013], as described below. Glacier and ice sheet projections are translated into RSL changes using static-equilibrium fingerprints for eighteen glacier regions, the Greenland Ice Sheet, the West Antarctic Ice Sheet (WAIS), and the East Antarctic Ice Sheet (EAIS) [Mitrovica *et al.*, 2011].

Bamber and Aspinall [2013] elicited from fourteen experts central 90% probability estimates for the rate of GMSL rise in 2100 due to the Greenland ice sheet, WAIS and EAIS. They did not distinguish between surface-mass balance and dynamic contributions, nor did they distinguish between emissions scenarios. In turning these rates into cumulative 21st century GMSL rise contributions, they assumed a linear increase in rates based on the experts’ rate estimates for the last decade and for 2100.

AR5 assessed the likely (central 66% probability; see exegesis by *Church et al.* [2013b]) range of Greenland and Antarctic contributions in 2080–2099, distinguishing between surface-mass balance and dynamic terms. They did not distinguish between EAIS and WAIS. For the dynamic AIS contribution, they did not distinguish among RCPs.

K14 combined the *Bamber and Aspinall* [2013] and AR5 approaches in a manner intended to retain consistency with the likely ranges of AR5. In particular, K14: (1) calculated a probability distribution for EAIS, WAIS, and Greenland changes over time from *Bamber and Aspinall* [2013], assuming linear changes in rates; (2) calculated a probability distribution for AIS and Greenland over time based on the AR5 likely ranges for 2080–2099, again assuming linear changes in rates to achieve these values; (3) shifted the first set of distributions by a time-varying constant so the medians of the two sets agree; (4) separated the AR5-derived Antarctic distribution into EAIS and WAIS terms by assuming the EAIS/WAIS ratio is the same as in the median projection from the first set; and (5) applied multipliers (separately for values greater than and less than the median) to the difference of the values in the final distribution from the distribution’s median, so that the central 66% probability range matches that of AR5.

2.2 Revised Antarctic projections

In this paper, we compare two sets of projections. The first, which we label K14, follows the original methodology of K14, extended in space and time. The second, which we label DP16, replaces the AIS projections of K14 with projections based on new physical modeling [*DeConto and Pollard*, 2016] that considers glaciological processes not previously considered at the continental ice-sheet scale. These processes include the influence of surface meltwater, driven by summer temperatures above freezing and the increasing ratio of rain to snow in a warming climate, on the penetration into ice shelves of surface crevasses that can lead to hydrofracturing. Hence, in DP16, buttressing ice shelves can thin or be lost entirely due to sub-ice ocean warming, the extensive spread of surface meltwater, or a combination of the two. In places where thick, marine-terminating grounding lines have lost their buttressing ice shelves, a wastage rate of ice is applied locally at the tidewater grounding line in places where vertical ice cliffs are tall enough to produce stresses that exceed the yield strength of the ice (see *DeConto and Pollard* [2016] and *Pollard et al.* [2015] for complete formulation).

Three uncertain but key model parameters relate to (1) the rate of sub-ice shelf melt rates in response to warming ocean temperatures, (2) the sensitivity of crevasse penetration to meltwater input (hydrofracturing), and (3) the maximum rate of cliff collapse. Because, as discussed below, there are no modern analogues to widespread ice-cliff failure, model performance cannot be adequately judged relative to Holocene or recent trends in ice-sheet behavior. Instead, the new model physics were tested relative to past episodes of ice sheet retreat during the Pliocene (~3 Ma) and the Last Interglacial (LIG, ~125 Ma), when Antarctic ocean and surface air temperatures were warmer than today [*Capron et al.*, 2014; *Rovere et al.*, 2014]. The three key parameters were varied systematically. From an initial 64 versions of the ice sheet model, 29 were found to satisfy both Pliocene and LIG sea-level targets, with Antarctic contributions to GMSL ranging between 5 to 15 m (Pliocene) and 3.6 to 7.4 m (LIG). The range of oceanic melt rate model parameters passing the Pliocene and LIG sea-level tests are comparable to those determined from a large, 625-member ensemble of the last deglacial retreat of the West Antarctic Ice Sheet using the same ice sheet model [*Pollard et al.*, 2016]; however, the deglacial simulations do not provide guidance on hydrofracturing and ice-cliff physics, because the background climate was too cold to trigger those processes.

One challenge of formulating a parameterization of ice-cliff physics is the lack of observations of marine-terminating ice without buttressing ice shelves and of sufficient thickness (~1000 m) to allow subaerial ice cliffs tall enough (~100 m) to drive structural collapse [*Bassis and Walker*, 2011]. The few calving fronts of this scale that exist today (e.g., Hel-

heim and Jakobshavn Glaciers on Greenland, and Crane Glacier on the Antarctic Peninsula) are experiencing rates of calving and structural failure at the terminus, comparable to the seaward flow of the glaciers, on the order of ~ 2 to > 12 km/yr [e.g., *Howat et al.*, 2008; *Joughin et al.*, 2014; *Wuite et al.*, 2015]. These outlet glaciers are in relatively narrow (5–12 km wide), restricted fjords, with substantial melange and supportive, lateral shear along the fjord walls. Hence, using observed rates of cliff collapse to constrain the model physics representing these processes could lead to underestimates.

In Antarctica, there is potential for much wider ice cliffs to form along vast stretches of the coastline if floating ice tongues and shelves are lost. For example, the throat of Thwaites Glacier is about 120 km wide, but at present its grounding line is mostly on bedrock too shallow (about 600 m deep; *Millan et al.* [2017]) to drive extensive structural failure at the terminus [*Bassis and Walker*, 2011]. In the model, the maximum allowable rate of cliff collapse – the maximum horizontal rate of ice loss applied at the marine “tidewater” calving terminus where ice cliffs are tall enough to generate stresses that exceed the strength of the ice – is 5 km/yr. This rate is less than half the rate of mass wastage at the front of Jakobshavn, which currently has a relatively stable terminus position but is flowing seaward at > 12 km/year [*Joughin et al.*, 2012]. To include the potential for even faster rates of ice sheet mass loss than in the existing model formulation, future work should consider a wider range of parameter space.

We note that the paleo-sea-level targets used to test and calibrate the model physics provide limited guidance regarding potential rates of ice-sheet retreat. While *Kopp et al.* [2009] do provide an estimate of the rate of sea-level rise contributed by the Antarctic Ice Sheet during LIG retreat, both their temporal resolution and their ability to attribute GMSL changes to AIS are limited. Moreover, given limited Antarctic atmospheric warming during the LIG relative to the Pliocene, initial WAIS retreat was more likely driven by oceanic warming than atmospheric warming [*DeConto and Pollard*, 2016], and therefore offers little in terms of validating rates of retreat driven by extensive surface melt, hydrofracture, and cliff collapse.

As described in *DeConto and Pollard* [2016], the 29 versions of the ice sheet model satisfying modern and geological constraints were used to run equally weighted ensembles of future ice-sheet retreat following RCP 2.6, 4.5, and 8.5 greenhouse gas pathways. In the future simulations, time-evolving oceanic melt rates were driven by NCAR CCSM4 [*Gent et al.*, 2011; *Shields and Kiehl*, 2016] sub-surface ocean temperatures. Surface mass balance and meltwater production rates were calculated from monthly air temperatures and precipitation provided by the RegCM3 regional climate model [*Pal et al.*, 2007] run offline and bias-corrected relative to a modern climatology [*DeConto and Pollard*, 2016; *Le Brocq et al.*, 2010].

Coupled atmosphere-ocean models are known to struggle with subsurface ocean temperatures in the circum-Antarctic [*Little and Urban*, 2016]. To minimize the effects of a general cold bias in NCAR CCSM4 Antarctic Shelf Bottom Water in the Amundsen and Bellingshausen Seas, a correction of 3°C was applied to ocean temperatures at 400 m depth. This bias correction is meant to compensate for the recent warming observed there [*Schmidtke et al.*, 2014]. The correction is greater than the actual temperature offset, but given the formulation of the sub-ice melt rate parameterization used in DP16, a 3°C correction is required to bring modern oceanic sub-ice shelf melt rates closer to observations [*Rignot et al.*, 2013]. The effect of not using the ocean temperature/melt-rate correction in future simulations is shown in Supplementary Information.

2.3 Extensions of the spatial and temporal domain.

The projections framework in this paper has a more extended spatial domain than the original K14 projections. While the original K14 projections were generated only at the precise location of tide gauges, here we also generate projections at points on a $2^{\circ}\times 2^{\circ}$ -resolution

global grid that intersect world coastlines. At these points, we use the spatiotemporal statistical model described in K14 to estimate (with larger errors than at the tide-gauge sites) the long-term, non-climatic, background contribution to RSL change. The projection assumes that the background rate of change estimated from tide-gauge data continues unchanged over the duration of the projections.

The projection framework also has a more extended temporal domain than the original K14 projections. Whereas the original K14 projections end in 2200, here we generated projections to 2300. This extension requires no computational modifications to the K14 framework. However, we regard this time frame as more appropriate when considering projections in which Antarctic ice sheet behavior are determined by a physical model rather than by a simple quadratic projection.

2.4 Assessment of population exposure.

To assess the population occupying land threatened with submergence under different sea level rise projections, we threshold NASA's 1-arcsec SRTM 3.0 digital elevation model [NASA JPL, 2013], referenced to local mean higher-high water levels, against the K14 and DP16 projection grids. We intersect the resulting inundation surfaces with contemporary population [Bright *et al.*, 2011] and national boundary [Hijmans *et al.*, 2012] data to estimate current national populations occupying land at risk of permanent submergence. SRTM data are the most practical option and widely used for global coastal exposure research, but bias estimates low [Kulp and Strauss, 2016]. For each set of sea-level rise projections, we assess the population exposed assuming each grid cell followed its 50th, 5th, or 95th percentile RSL projection. Further details are provided in Supplementary Information.

3 Results

The K14 Antarctic projections – like those of Bamber and Aspinall [2013] and Little *et al.* [2013a,b], among others – assumed that changes in the rates of change in ice-sheet mass balance occurred linearly. For example, Bamber and Aspinall [2013] elicited expert opinion on the rate of Antarctic ice sheet mass change in 2100, and assumed that the elicited rate was achieved following a linear growth rate. The result is a quadratic change in ice volume. K14 took the same approach (Figures 1 and 2). By contrast, process modeling as in DP16 shows considerably more complex behavior, with periods of rapid increases in mass loss rate as sectors of ice sheet collapse, and other intervals of stable or declining rates (Figure 1).

In the first half of the 21st century, the range spanned by DP16 projections is similar to that spanned by K14 (-10 to +23 cm in 2050, vs. a 1st–99th percentile range of -2 to +14 cm under K14). Both sets of projections show minimal emissions-scenario dependency in the first half of the 21st century. The central tendency among the DP16 projections is slightly higher, with a median of about +5 cm under DP16, compared to a median of +2 cm under K14. These slightly higher values are driven by the ocean-temperature bias correction, which is needed to improve consistency with observed oceanic sub-ice melt rates in the Amundsen and Bellingshausen Sea sectors of West Antarctica [Rignot *et al.*, 2013]. Without this correction, there is a tendency toward Antarctic growth in the early decades of the century (in 2050, RCP 8.5: median -3 cm, range of -9 to +12 cm, RCP 2.6: median -2 cm, range of -10 to +6 cm). However, even with the bias correction, Antarctica's median contribution to GMSL is still 0.1 mm/yr, which is about a factor of 3 less than that currently observed for the early 21st-century [Shepherd *et al.*, 2012; Church *et al.*, 2013a; Harig and Simons, 2015]. Overall, the substitution of DP16 has a very limited effect on mid-century GMSL projections (Table 1).

Under strong forcing, the overall picture changes dramatically by the end of the 21st century, with several of the DP16 simulations leading to AIS contributions to GMSL exceed-

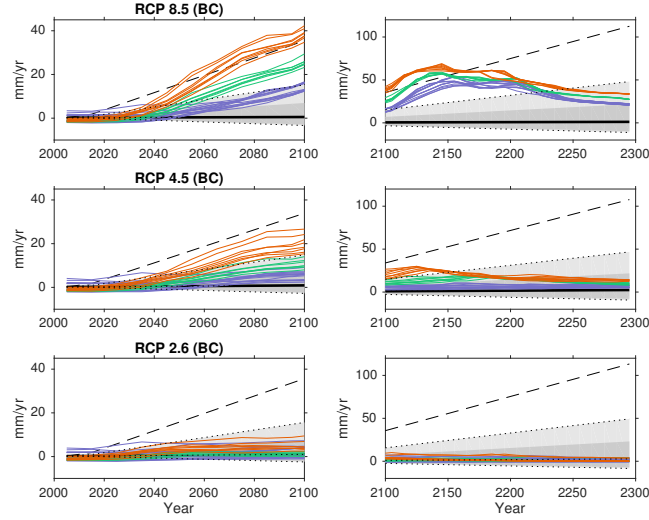


Figure 1. Rates of change of Antarctic ice sheet mass under the three RCPs. Dark/light shaded areas represent 5–95th and 0.5th–99.5th percentile of K14. Dashed black line represents 99.9th percentile of K14. Colored curves are DP16 runs, with colors for visibility reflecting different levels of melt in 2100 under RCP 8.5. Left panels show 2000–2100, right panels show 2100–2300. Note change of horizontal and vertical scales.

ing +1 m by 2100 under RCP 8.5 (Figure 2). As a consequence, the median DP16 GMSL projections for 2100 under RCP 8.5 reaches 146 cm, the 98th percentile projection under K14. The low tail is curtailed by the incorporation of physical modeling, with a 1st percentile of 80 cm exceeding the median of K14. DP16 RSL projections indicate the risk of significant changes to the global coastline by 2100. Without protective measures, the 5th–95th percentiles of RSL projections under DP16 would inundate land currently home to 54–132 million people. This contrasts with 54–79 million people under the K14 projections (Table 2, full table in Data Set 6).

A significant enhancement of the AIS contribution to GMSL also occurs for 2100 under moderate forcing: the median DP16 GMSL projections of 91 cm under RCP 4.5 is consistent with the 93rd percentile of K14. The low tail is modestly curtailed: the DP16 1st–99th percentile values for RCP 4.5 (39–180 cm) resemble the K14 9th–99.8th percentile range. Under low forcing (RCP 2.6), there is little effect, with the DP16 1st–99th percentile range (18–111 cm) resembling the K14 0.5th–99th percentile range.

These differences build over the 22nd and 23rd century. By 2300, under RCP 8.5, the median DP16 GMSL projection of 11.7 m exceeds the K14 99th percentile. Without protective measures, median DP16 RSL projections would submerge land currently home to 900 million people worldwide, a roughly five-fold increase relative to K14 (Table 2). The DP16 1st–99th percentile range (8.6–17.5 m) resembles the K14 97th–99.8th percentile range. Under RCP 4.5, the median DP16 GMSL projection of 4.2 m resembles the K14 90th percentile, and the DP16 1st–99th percentile range (1.6–8.1 m) resembles the K14 42nd–98th percentile range. Under RCP 2.6, by contrast, the median DP16 GMSL projection of 1.4 m matches the K14 median, and the DP16 1st–99th percentile range (0.2–4.0 m) resembles the K14 14th–92nd percentile range.

Taken together, the incorporation of the DP16 AIS ensemble pulls the projections much higher by 2100 and beyond under RCP 4.5 and especially RCP 8.5. It thus leads to a significant reduction in overlap among projections of GMSL change based upon different emissions scenarios. This is to be expected based on the difference in construction between

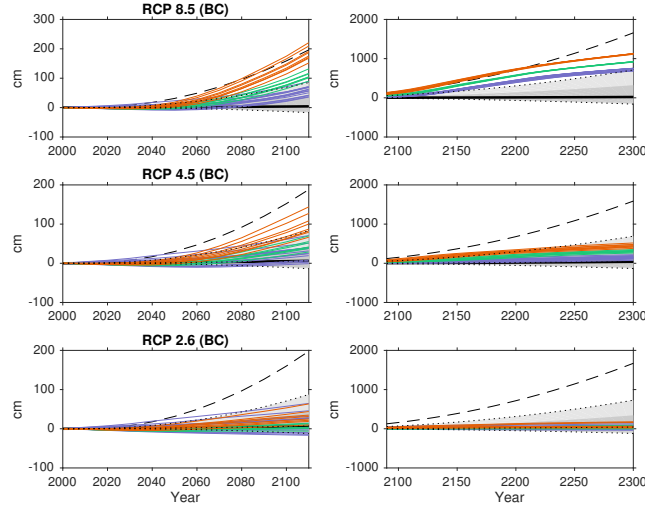


Figure 2. Antarctic ice sheet projections under the three RCPs. Dark/light shaded areas represent 5–95th and 0.5th–99.5th percentile of K14. Dotted black line represents 99.9th percentile of K14. Colored curves are DP16 runs, with colors for visibility reflecting different levels of melt in 2100 under RCP 8.5. Left panels show 2000–2100, right panels show 2100–2300. Note change of horizontal and vertical scales.

the K14 Antarctic projections and the DP16 projections. In K14, as in AR5, AIS surface mass balance is scenario-dependent, but the ice-sheet dynamic term is treated as scenario-independent: it is assumed that the uncertainty in physical understanding of ice-sheet behavior swamps the forcing uncertainty. By contrast, the physical model of DP16 yields a strong forcing dependence.

As a consequence of this difference, the proportion of total projection variance attributable to emissions changes significantly with the incorporation of the DP16 ensemble. Under K14, relative to RCP 4.5, thermal expansion is initially the dominant contributor to projection variance (accounting for about 70% of total variance in 2020). By 2060, AIS accounts for one-third of total variance and is the single largest contributor. The AIS share grows over time, accounting for more than 60% of total variance by 2300. Assuming RCP 2.6, 4.5 and 8.5 are all treated as equally likely, scenario uncertainty accounts for only ~10% of total variance in 2050, a share that grows to 20–30% by 2070 and stays in this range through 2300.

Under DP16, physical uncertainty in AIS initially dominates total variance (89% in 2020). This share declines over time, predominantly losing out to emissions scenario uncertainty, which grows from 8% of total variance in 2050, to 45% in 2070, to 65% in 2100, and continues to grow to 89% in 2250. This shift reflects the larger sensitivity of the DP16 AIS projections to emissions scenario.

The assumption of a simple linear change in rate of mass loss underlying K14 leads to a perfect correlation between the rate of AIS mass loss observed in the near term and that projected for the long term (Figure 5). If this assumption were correct, knowing that AIS mass loss in the first decades of this century fell in the middle of the estimated distribution would rule out high-end mass loss late in the century or beyond. By contrast, DP16 projections reveal no correlation between the AIS contribution to GMSL in 2020 and that in 2100 ($r = -0.08$, pooling across RCPs and both with and without an ocean temperature adjustment), and only a weak correlation between the AIS contribution in 2050 and in 2100 ($r = 0.26$). In the second half of the century, observed AIS behavior becomes more strongly

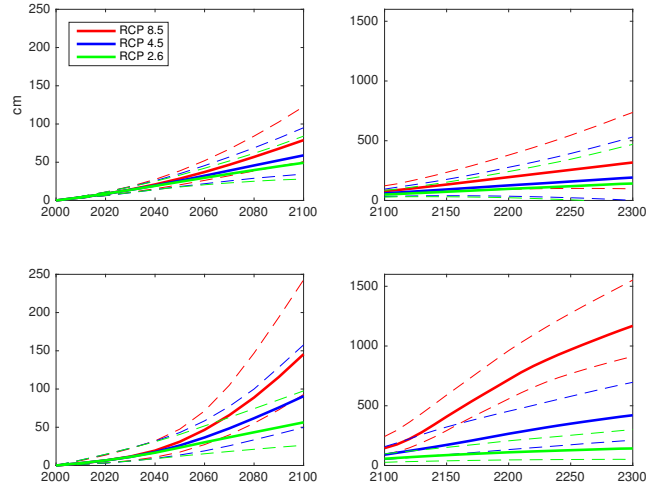


Figure 3. Projections of GMSL rise for the three RCPs under K14 (top row) and DP16 (bottom row). Heavy = median, dashed=5th–95th percentile. Left panels show 2000–2100, right panels show 2100–2300. Note change of horizontal and vertical scales.

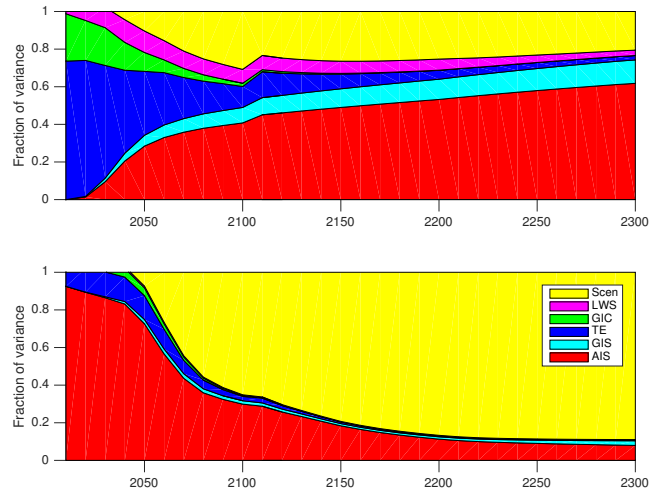


Figure 4. Contributions to the variance in GMSL over time under K14 (top) and DP16 (bottom), relative to RCP 4.5. The discontinuity between 2100 and 2110 is due to the reduction in the number of CMIP5 model simulations available beyond 2100.

predictive of long-term behavior; the correlation with the AIS contribution to 2300 grows from $r = 0.26$ in 2050 to $r = 0.82$ in 2100, $r = 0.97$ in 2150, and $r = 0.997$ in 2200.

The general lack of correlation between the AIS contributions in 2020 and 2100, and the rapidly strengthening correlations in the second half of the 21st century, are caused by a transition in the model from an ocean-dominated driver of ice-shelf loss (and reduced buttressing) to an atmosphere-dominated driver via hydrofracturing. If parametric tuning of the model performance relative to paleo-sea-level targets were limited to oceanic melt rates, we would expect to see better coherence between model trends at 2020 and 2100.

The effect of DP16 on RSL projections is as would be expected based on the change in projected WAIS and EAIS contributions and their associated static-equilibrium fingerprints (Figures 6, S8, and S9). Relative to K14, the effect on RSL projections for 2050 is

Table 1. Projections of GMSL rise (cm)

	50	17–83	5–95	1–99	99.9
K14					
RCP 8.5					
2050	29	24–34	21–39	17–46	59
2100	79	62–101	51–123	40–159	232
2200	195	131–284	94–380	64–552	886
2300	318	175–516	98–737	37–1093	1929
RCP 4.5					
2050	26	21–31	18–35	15–41	55
2100	59	44–77	35–95	26–128	205
2200	126	70–197	36–278	8–433	780
2300	192	70–349	0–531	-55–900	1717
RCP 2.6					
2050	24	20–29	18–33	15–40	55
2100	49	36–66	28–84	20–120	203
2200	97	48–163	23–242	6–406	803
2300	142	32–288	-22–470	-57–847	1773
DP16					
RCP 8.5					
2050	31	22–40	17–48	13–54	59
2100	146	109–209	93–243	80–267	297
2200	719	595–896	558–962	525–1049	1193
2300	1169	980–1409	913–1552	861–1751	2006
RCP 4.5					
2050	26	18–36	14–43	10–52	57
2100	91	66–125	50–158	39–180	197
2200	266	176–396	133–455	102–510	594
2300	421	275–595	211–696	163–806	995
RCP 2.6					
2050	23	16–33	12–41	9–50	54
2100	56	37–78	26–98	18–111	122
2200	110	70–161	47–206	30–250	314
2300	142	83–230	50–300	22–404	552

Columns indicate percentiles of frequency distributions.

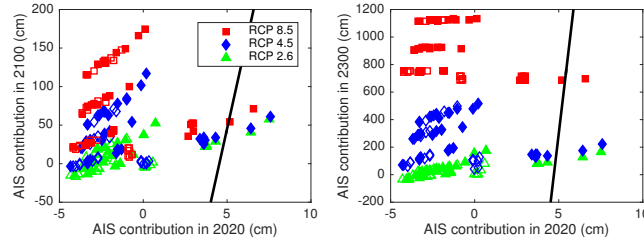


Figure 5. Relationship between the Antarctic ice sheet contribution to GMSL in 2020 and that in 2100 (left) or 2300 (right). Black line is the relationship in the K14 projections. Red/blue/green is the DP16 ensemble (red = RCP 8.5; blue = RCP 4.5; green = RCP 2.6; filled = with bias correction; open = without bias correction).

minimal (< 4 cm). By 2100, however, the increase in median AISL contribution decreases projected RSL rise in the Antarctic, while enhancing it most strongly in a geographic swath including North America, the central Pacific, Australia, southeast Asia, and parts of India and Africa same. (Detailed frequency distributions of RSL at tide gauge sites and on the global grid are provided in the Supplementary Information.)

4 Discussion and Conclusions

The replacement of the probabilistic, expert-assessment- and expert-elicitation-based AIS projections of K14 with the physical-model-based projections of DP16 leads to a number of significant effects on GMSL and RSL projections.

Table 2. Population exposure (millions of people)

Population exposure under 2100 RSL projections					
Region	Total Pop.	RCP 2.6/K14	RCP 2.6/DP16	RCP 8.5/K14	RCP 8.5/DP16
World	6,836.4	47.1 (36.5–65.0)	48.8 (37.6–67.0)	54.0 (42.1–78.5)	79.2 (54.0–132.0)
China	1,330.2	7.9 (5.2–12.1)	8.1 (5.4–12.6)	8.8 (6.2–15.1)	14.6 (8.4–26.8)
Bangladesh	156.1	0.9 (0.5–1.6)	1.0 (0.6–1.6)	1.2 (0.7–2.2)	2.2 (1.2–5.0)
India	1,173.2	2.2 (1.6–3.0)	2.3 (1.6–3.1)	2.5 (1.9–3.9)	4.1 (2.5–7.6)
Indonesia	242.9	1.2 (0.8–2.1)	1.3 (0.8–2.2)	1.5 (0.9–2.9)	2.9 (1.5–6.0)
Vietnam	895.5	3.8 (2.9–6.3)	3.9 (3.0–6.4)	4.8 (3.6–7.0)	6.8 (4.7–12.1)

Population exposure under 2300 RSL projections					
Region	Total Pop.	RCP 2.6/K14	RCP 2.6/DP16	RCP 8.5/K14	RCP 8.5/DP16
World	6,836.4	81.9 (25.2–363.7)	82.9 (38.6–226.1)	182.0 (47.9–608.1)	900.6 (680.6–1,127.0)
China	1,330.2	13.9 (2.9–79.3)	14.0 (4.7–50.2)	36.5 (5.5–138.4)	185.4 (138.9–229.4)
Bangladesh	156.1	7.0 (1.2–39.8)	7.1 (2.2–23.2)	19.0 (3.3–71.3)	103.0 (79.9–121.6)
India	1,173.2	4.6 (1.1–25.5)	4.7 (1.9–14.1)	11.6 (2.6–52.8)	93.0 (60.8–124.7)
Indonesia	242.9	2.5 (0.4–21.4)	2.5 (0.6–12.2)	8.0 (0.8–41.3)	60.8 (45.2–76.8)
Vietnam	895.5	6.6 (1.4–27.4)	6.6 (2.5–19.2)	15.0 (3.0–43.0)	54.3 (44.7–60.6)

Population currently living in land at risk of permanent inundation based on median (5th–95th percentile) RSL projections.

Population densities based on 2010 estimates.

The top five countries with the most exposure in 2300 under median RCP 8.5/DP16 are included in this table.

First, the novel ice-shelf-hydrofracturing and ice-cliff-collapse mechanisms in DP16 lead to a significant upward shift in central projections for strong (RCP 8.5) and moderate (RCP 4.5) forcing scenarios. The DP16 simulations provide physically meaningful pathways that can lead to > 2.0 m of total GMSL rise by 2100 under RCP 8.5 and > 1.5 m under RCP 4.5 [Oppenheimer and Alley, 2016; Sweet *et al.*, 2017]. That said, end-users of sea-level rise projections should be cognizant of single-study bias: these simulations should be viewed as expanding scientific understanding of the space of the physically coherent, rather than as offering firm projections of what will be.

There remain important physical processes that are not currently modeled but could be critical for the timing and pace of major ice-sheet retreat. For example, at present, continental-scale ice-sheet models poorly represent the meltwater-buffering capacity of firn, the transitional layer between newer snow and underlying ice. In the future, as summer air temperatures begin to drive the production of more rain and surface melt, meltwater will be absorbed by the firn layer as long as the layer contains uncompacted pore space, limiting the meltwater’s potential to flow into crevasses and hydrofracture the underlying ice [Munneke *et al.*, 2014].

The breadth of published projections, as well as of remaining structural uncertainties, highlight the fact that future SLR remains an arena of deep uncertainty [Kasperson, 2008; Heal and Millner, 2014]. For the foreseeable future, there will not be a single, uniquely valid approach for estimating the probability of different levels of future change. End-users should therefore consider applying adaptive management and/or robust decision frameworks appropriate for deeply uncertain contexts. For example, end-users could try to structure decisions in a staged fashion, such that the decisions being made today depend upon relatively well-constrained mid-century projections while leaving open a variety of options for later in the century [e.g., Ranger *et al.*, 2013].

Alternatively, where decisions relying on late-century projections cannot be avoided, end-users could rely on strategies that maximize utility or minimize regret across multiple possible probability distributions [e.g., Heal and Millner, 2014]. One simple multiple-probability-distribution approach involves giving special consideration to physically plausible but low-likelihood projections in the high-end tail of projected probability distributions [e.g., Buchanan *et al.*, 2016]. K14 suggested that the 99.9th percentile of their projection for RCP 8.5, which yielded ~2.5 m of GMSL rise by 2100, represented a physically plau-

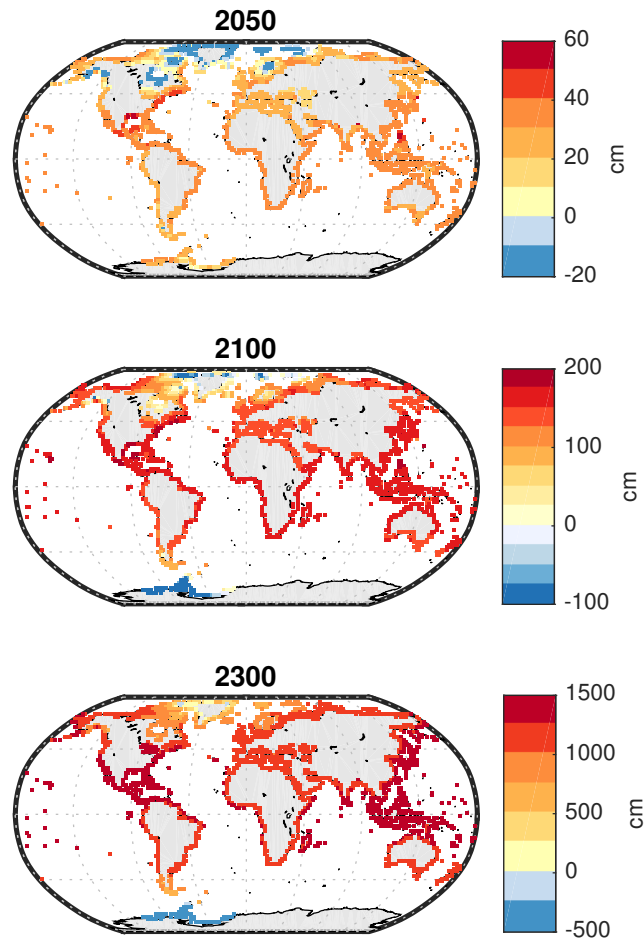


Figure 6. Median DP16 RSL projections under RCP 8.5 in 2050, 2100 and 2300.

sible ‘worst case.’ The highest values from the DP16 projections are only modestly higher, although high values occur with greater frequency: under RCP 8.5, the DP16 ensemble revises the frequency of a 2.5 m GMSL rise upward from $\sim 0.1\%$ to $\sim 0.6\%$. However, the DP16 ensemble was not generated using carefully constructed parameter priors, and there is no good reason to conclude that it covers the full space of plausible outcomes. Notably, rates of ice-cliff collapse faster than the 5 km/yr maximum of DP16 have been observed in parts of Greenland, and faster rates of ice-cliff collapse would yield faster rates of ice-sheet shrinkage.

Second, in the second half of this century and beyond, sea-level projections incorporating the DP16 ensemble are significantly more forcing-sensitive than the K14 projections. Due primarily to the significant number of simulations involving collapse of parts of AIS under strong forcing, the gap in the median GMSL projection for 2100 between RCP 8.5 and RCP 2.6 grows from 30 cm under K14 to 90 cm under the projections under DP16. Under RCP 2.6 and DP16, the 99th percentile projection remains below 2 m through 2200. If these findings are correct, they point to a significantly larger mitigation benefit than indicated by the AR5 or K14 sea-level projections.

Third, the DP16 projections indicate a much weaker correlation between the near-term behavior of AIS and its contribution to GMSL rise over the course of this century and beyond. Finding the planet on a ‘moderate’ sea-level rise pathway over the first half of the 21st century cannot exclude ‘extreme’ outcomes subsequently. For end-users employing

discrete scenarios of sea-level rise, such as those constructed by *Sweet et al.* [2017], this means that ‘extreme’ future scenarios need to be considered even if they overestimate current rates of sea-level rise. Constraining the future behavior of the AIS will require more detailed process-based modeling than the simple relationships used by *Bamber and Aspinall* [2013], K14, and others would indicate. It will also require a more thorough exploration of parameter space, and more physically based representations of key processes, including structural cliff failure. Currently, the potential for model intercomparisons is hampered by the lack of representations of these processes in other continental-scale models.

Moving forward, the development of probabilistic ice-sheet models that incorporate ice-sheet instabilities in a manner consistent with more detailed ice-sheet models is a key challenge for sea-level risk assessment. Such probabilistic models will enable estimation of sea-level rise probabilities that reflect emissions sensitivity and the potential for rapid increases in discharge rate more accurately than current approaches. Probabilistic projections are a valuable input into the design of projects and policies intended to manage coastal flood risk [e.g., *Buchanan et al.*, 2016; *Lempert et al.*, 2012; *Wong et al.*, 2016; *Oppenheimer and Alley*, 2016], as well as assessments of the value of climate change mitigation [e.g., *Hinkel et al.*, 2014; *Houser et al.*, 2015; *Diaz*, 2016]. They will also enable value-of-information analyses, which can inform the design of observation systems intended to reduce the key physical uncertainties underlying future sea-level projections [*Cooke et al.*, 2014].

Probabilistic assessment also requires more research on potential bounds for factors that influence the AIS. For example, it is unclear whether even a full ensemble of GCMs would fully constrain the range of plausible distributions of near surface ocean temperature, sea ice, and storm tracks near the AIS. More research is also needed on interactions and feedbacks across the AIS and between the AIS and the rest of the world, including through poorly understood mechanisms like ocean circulation that could over long time scales influence other drivers of coastal flood risk (such as tropical cyclones) around the globe.

Acknowledgments

REK was supported in part by a grant from Rhodium Group (for whom he has previously worked as a consultant), as part of the Climate Impact Lab consortium. RMD and DP were supported by grants from the National Science Foundation under the OCE 1202632 PlioMAX and AGS 1203910/1203792. This paper is a contribution to PALSEA2 (Palaeo-Constraints on Sea-Level Rise), which is a working group of Past Global Changes/IMAGES (International Marine Past Global Change Study) and an International Focus Group of the International Union for Quaternary Research. We acknowledge the World Climate Research Programme’s Working Group on Coupled Modeling, which is responsible for CMIP, and we thank the climate modeling groups (listed in Table S1) for producing and making available their model output. For CMIP, the U.S. Department of Energy’s Program for Climate Model Diagnosis and Intercomparison provides coordinating support and led development of software infrastructure in partnership with the Global Organization for Earth System Science Portals. Code for generating sea-level projections is available in the ProjectSL (<https://github.com/bobkopp/ProjectSL>) and LocalizeSL (<https://github.com/bobkopp/LocalizeSL>) repositories on Github.

References

- AVISO (2011), MSS_CNES_CLS2011.
- Bamber, J. L., and W. P. Aspinall (2013), An expert judgement assessment of future sea level rise from the ice sheets, *Nature Climate Change*, 3, 424–427, doi:10.1038/nclimate1778.
- Bassis, J., and C. Walker (2011), Upper and lower limits on the stability of calving glaciers from the yield strength envelope of ice, *Proceedings of the Royal Society A*, p. rspa20110422, doi:10.1098/rspa.2011.0422.
- Bright, E. A., P. R. Coleman, A. N. Rose, and M. L. Urban (2011), LandScan 2010.

- Buchanan, M. K., R. E. Kopp, M. Oppenheimer, and C. Tebaldi (2016), Allowances for evolving coastal flood risk under uncertain local sea-level rise, *Climatic Change*, 137, 347–362, doi:10.1007/s10584-016-1664-7.
- Capron, E., A. Govin, E. J. Stone, V. Masson-Delmotte, S. Mulitza, B. Otto-Bliesner, T. L. Rasmussen, L. C. Sime, C. Waelbroeck, and E. W. Wolff (2014), Temporal and spatial structure of multi-millennial temperature changes at high latitudes during the last interglacial, *Quaternary Science Reviews*, 103, 116–133, doi:10.1016/j.quascirev.2014.08.018.
- Cayan, D. R., J. Kalansky, S. Iacobellis, and D. Pierce (2016), Creating probabilistic sea level rise projections, *Tech. Rep. TN 211806*, California Energy Commission.
- Chao, B. F., Y. H. Wu, and Y. S. Li (2008), Impact of artificial reservoir water impoundment on global sea level, *Science*, 320(5873), 212–214, doi:10.1126/science.1154580.
- Church, J. A., P. U. Clark, et al. (2013a), Chapter 13: Sea level change, in *Climate Change 2013: the Physical Science Basis*, edited by T. F. Stocker, D. Qin, et al., Intergovernmental Panel on Climate Change.
- Church, J. A., P. U. Clark, A. Cazenave, J. M. Gregory, S. Jevrejeva, A. Levermann, M. A. Merrifield, G. A. Milne, R. S. Nerem, P. D. Nunn, et al. (2013b), Sea-level rise by 2100, *Science*, 342(6165), 1445–1445, doi:10.1126/science.342.6165.1445-a.
- Cooke, R., B. A. Wielicki, D. F. Young, and M. G. Mlynarczyk (2014), Value of information for climate observing systems, *Environment Systems and Decisions*, 34(1), 98–109, doi:10.1007/s10669-013-9451-8.
- DeConto, R. M., and D. Pollard (2016), Contribution of antarctica to past and future sea-level rise, *Nature*, 531(7596), 591–597, doi:10.1038/nature17145.
- Diaz, D. B. (2016), Estimating global damages from sea level rise with the Coastal Impact and Adaptation Model (CIAM), *Climatic Change*, 137(1), 143–156, doi:10.1007/s10584-016-1675-4.
- Douglas, E., P. Kirshen, R. Hannigan, R. Herst, A. Palardy, R. DeConto, D. FitzGerald, C. Hay, Z. Hughes, A. Kemp, R. Kopp, B. Anderson, Z. Kuang, S. Ravela, J. Woodruff, M. Barlow, M. Collins, A. DeGaetano, C. A. Schlosser, A. Ganguly, E. Kodra, and M. Ruth (2016), *Climate Change and Sea Level Rise Projections for Boston: the Boston Research Advisory Group Report*, 54 pp. pp., Climate Ready Boston, Boston, MA.
- Egbert, G. D., and S. Y. Erofeeva (2002), Efficient inverse modeling of barotropic ocean tides, *Journal of Atmospheric and Oceanic Technology*, 19(2), 183–204, doi:10.1175/1520-0426(2002)019<0183:EIMOB>2.0.CO;2.
- Gent, P. R., G. Danabasoglu, L. J. Donner, M. M. Holland, E. C. Hunke, S. R. Jayne, D. M. Lawrence, R. B. Neale, P. J. Rasch, M. Vertenstein, et al. (2011), The Community Climate System Model version 4, *Journal of Climate*, 24(19), 4973–4991, doi:10.1175/2011JCLI4083.1.
- Hargis, C., and F. J. Simons (2015), Accelerated west antarctic ice mass loss continues to outpace east antarctic gains, *Earth and Planetary Science Letters*, 415, 134–141, doi:10.1016/j.epsl.2015.01.029.
- Heal, G., and A. Millner (2014), Reflections uncertainty and decision making in climate change economics, *Review of Environmental Economics and Policy*, 8(1), 120–137, doi:10.1093/reep/ret023.
- Hijmans, R., J. Kapoor, J. Wiczorek, N. Garcia, A. Maunahan, A. Rala, and A. Mandel (2012), GADM database of Global Administrative Areas 2.0.
- Hinkel, J., D. Lincke, A. T. Vafeidis, M. Perrette, R. J. Nicholls, R. S. Tol, B. Marzeion, X. Fettweis, C. Ionescu, and A. Levermann (2014), Coastal flood damage and adaptation costs under 21st century sea-level rise, *Proceedings of the National Academy of Sciences*, 111(9), 3292–3297, doi:10.1073/pnas.1222469111.
- Houser, T., S. Hsiang, R. Kopp, and K. Larsen (2015), *Economic Risks of Climate Change: An American Prospectus*, 376 pp. pp., Columbia University Press, New York.
- Howat, I. M., I. Joughin, M. Fahnestock, B. E. Smith, and T. A. Scambos (2008), Synchronous retreat and acceleration of southeast greenland outlet glaciers 2000–06: Ice dynamics and coupling to climate, *Journal of Glaciology*, 54(187), 646–660, doi:10.3189/

- 002214308786570908.
- Jackson, L. P., and S. Jevrejeva (2016), A probabilistic approach to 21st century regional sea-level projections using RCP and High-end scenarios, *Global and Planetary Change*, 146, 179–189, doi:10.1016/j.gloplacha.2016.10.006.
- Joughin, I., B. E. Smith, I. M. Howat, D. Floricioiu, R. B. Alley, M. Truffer, and M. Fahnestock (2012), Seasonal to decadal scale variations in the surface velocity of Jakobshavn Isbræ, Greenland: Observation and model-based analysis, *Journal of Geophysical Research: Earth Surface*, 117(F2), F02,030, doi:10.1029/2011JF002110.
- Joughin, I., B. E. Smith, and B. Medley (2014), Marine Ice Sheet Collapse Potentially Underway for the Thwaites Glacier Basin, West Antarctica, *Science*, 344, 735–738, doi:10.1126/science.1249055.
- Kasperson, R. E. (2008), Coping with deep uncertainty: Challenges for environmental assessment and decision making, in *Uncertainty and risk: Multidisciplinary perspectives*, edited by G. Bammer and M. Smithson, pp. 337–347, Earthscan, London.
- Konikow, L. F. (2011), Contribution of global groundwater depletion since 1900 to sea-level rise, *Geophysical Research Letters*, 38, L17,401, doi:10.1029/2011GL048604.
- Kopp, R. E., F. J. Simons, J. X. Mitrovica, A. C. Maloof, and M. Oppenheimer (2009), Probabilistic assessment of sea level during the last interglacial stage, *Nature*, 462(7275), 863–867, doi:10.1038/nature08686.
- Kopp, R. E., R. M. Horton, C. M. Little, J. X. Mitrovica, M. Oppenheimer, D. J. Rasmussen, B. H. Strauss, and C. Tebaldi (2014), Probabilistic 21st and 22nd century sea-level projections at a global network of tide gauge sites, *Earth's Future*, 2, 383–406, doi:10.1002/2014EF000239.
- Kopp, R. E., A. C. Kemp, K. Bitterman, B. P. Horton, J. P. Donnelly, W. R. Gehrels, C. C. Hay, J. X. Mitrovica, E. D. Morrow, and S. Rahmstorf (2016), Temperature-driven global sea-level variability in the Common Era, *Proceedings of the National Academy of Sciences*, 113, E1434–E1441, doi:10.1073/pnas.1517056113.
- Kulp, S., and B. H. Strauss (2016), Global DEM errors underpredict coastal vulnerability to sea level rise and flooding, *Frontiers in Earth Science*, 4, 10.3389/feart.2016.00.036, doi:10.3389/feart.2016.00036.
- LaLonde, T., A. Shortridge, and J. Messina (2010), The Influence of Land Cover on Shuttle Radar Topography Mission (SRTM) Elevations in Low-Relief Areas, *Transactions in GIS*, 14, 461–479, doi:10.1111/j.1467-9671.2010.01217.x.
- Le Brocq, A. M., A. J. Payne, and A. Vieli (2010), An improved antarctic dataset for high resolution numerical ice sheet models (albmap v1), *Earth system science data*, 2(2), 247–260, doi:10.5194/essd-2-247-2010.
- Lempert, R. J., R. L. Sriver, and K. Keller (2012), Characterizing Uncertain Sea Level Rise Projections to Support Investment Decisions, *Public Interest Energy Research Program White Paper CEC-500-2012-056*, California Energy Commission.
- Little, C. M., and N. M. Urban (2016), Cmp5 temperature biases and 21st century warming around the antarctic coast, *Annals of Glaciology*, 57, 69–78, doi:10.1017/aog.2016.25.
- Little, C. M., M. Oppenheimer, and N. M. Urban (2013a), Upper bounds on twenty-first-century antarctic ice loss assessed using a probabilistic framework, *Nature Climate Change*, 3(7), 654–659, doi:10.1038/nclimate1845.
- Little, C. M., N. M. Urban, and M. Oppenheimer (2013b), Probabilistic framework for assessing the ice sheet contribution to sea level change, *Proceedings of the National Academy of Sciences*, 110(9), 3264–3269, doi:10.1073/pnas.1214457110.
- Marzeion, B., A. H. Jarosch, and M. Hofer (2012), Past and future sea-level change from the surface mass balance of glaciers, *The Cryosphere*, 6, 1295–1322.
- Mengel, M., A. Levermann, K. Frieler, A. Robinson, B. Marzeion, and R. Winkelmann (2016), Future sea level rise constrained by observations and long-term commitment, *Proceedings of the National Academy of Sciences*, 113(10), 2597–2602, doi:10.1073/pnas.1500515113.

- Millan, R., E. Rignot, V. Bernier, M. Morlighem, and P. Dutrieux (2017), Bathymetry of the amundsen sea embayment sector of west antarctica from operation icebridge gravity and other data, *Geophysical Research Letters*, 44(3), 1360–1368, doi:10.1002/2016GL072071.
- Mitrovica, J. X., N. Gomez, E. Morrow, C. Hay, K. Latychev, and M. E. Tamisiea (2011), On the robustness of predictions of sea level fingerprints, *Geophysical Journal International*, 187(2), 729–742, doi:10.1111/j.1365-246X.2011.05090.x.
- Munneke, P. K., S. R. Ligtenberg, M. R. Van Den Broeke, and D. G. Vaughan (2014), Firn air depletion as a precursor of Antarctic ice-shelf collapse, *Journal of Glaciology*, 60(220), 205–214, doi:10.3189/2014JoG13J183.
- NASA JPL (2013), NASA Shuttle Radar Topography Mission Global 1 arc second [Data set], NASA LP DAAC, doi:10.5067/MEaSURES/SRTM/SRTMGL1.003.
- Oppenheimer, M., and R. B. Alley (2016), How high will the seas rise?, *Science*, 354(6318), 1375–1377, doi:10.1126/science.aak9460.
- Pal, J. S., F. Giorgi, X. Bi, N. Elguindi, F. Solmon, S. A. Rauscher, X. Gao, R. Francisco, A. Zakey, J. Winter, et al. (2007), Regional climate modeling for the developing world: the ICTP RegCM3 and RegCNET, *Bulletin of the American Meteorological Society*, 88(9), 1395–1409, doi:10.1175/BAMS-88-9-1395.
- Pollard, D., R. M. DeConto, and R. B. Alley (2015), Potential antarctic ice sheet retreat driven by hydrofracturing and ice cliff failure, *Earth and Planetary Science Letters*, 412, 112–121, doi:10.1016/j.epsl.2014.12.035.
- Pollard, D., W. Chang, M. Haran, P. Applegate, and R. DeConto (2016), Large ensemble modeling of the last deglacial retreat of the West Antarctic Ice Sheet: comparison of simple and advanced statistical techniques, *Geoscientific Model Development*, 9(5), 1697–1723, doi:10.5194/gmd-9-1697-2016.
- Rahmstorf, S., M. Perrette, and M. Vermeer (2012), Testing the robustness of semi-empirical sea level projections, *Climate Dynamics*, 39(3-4), 861–875.
- Ranger, N., T. Reeder, and J. Lowe (2013), Addressing ‘deep’ uncertainty over long-term climate in major infrastructure projects: four innovations of the Thames Estuary 2100 Project, *EURO Journal on Decision Processes*, 1(3-4), 233–262, doi:10.1007/s40070-013-0014-5.
- Rignot, E., S. Jacobs, J. Mouginot, and B. Scheuchl (2013), Ice-shelf melting around antarctica, *Science*, 341(6143), 266–270, doi:10.1126/science.1235798.
- Rodriguez, E., C. Morris, J. Belz, E. Chapin, J. Martin, W. Daffer, and S. Hansley (2005), An assessment of the SRTM topographic products, Technical Report JPL D-31639.
- Rovere, A., M. E. Raymo, J. Mitrovica, P. Hearty, M. O Leary, and J. Inglis (2014), The mid-pliocene sea-level conundrum: Glacial isostasy, eustasy and dynamic topography, *Earth and Planetary Science Letters*, 387, 27–33, doi:10.1016/j.epsl.2013.10.030.
- Schmidtko, S., K. J. Heywood, A. F. Thompson, and S. Aoki (2014), Multidecadal warming of Antarctic waters, *Science*, 346(6214), 1227–1231, doi:10.1126/science.1256117.
- Shepherd, A., E. R. Ivins, G. A. V. R. Barletta, M. J. Bentley, S. Bettadpur, K. H. Briggs, D. H. Bromwich, R. Forsberg, N. Galin, M. Horwath, S. Jacobs, I. Joughin, M. A. King, J. T. M. Lenaerts, J. Li, S. R. M. Ligtenberg, A. Luckman, S. B. Luthcke, M. McMillan, R. Meister, G. Milne, J. Mouginot, A. Muir, J. P. Nicolas, J. Paden, A. J. Payne, H. Pritchard, E. Rignot, H. Rott, L. S. Sørensen, T. A. Scambos, B. Scheuchl, E. J. O. Schrama, B. Smith, A. V. Sundal, J. H. v. Angelen, W. J. v. d. Berg, M. R. v. d. Broeke, D. G. Vaughan, I. Velicogna, J. Wahr, P. L. Whitehouse, D. J. Wingham, D. Yi, D. Young, and H. J. Zwally (2012), A reconciled estimate of ice-sheet mass balance, *Science*, 338(6111), 1183–1189, doi:10.1126/science.1228102.
- Shields, C. A., and J. T. Kiehl (2016), Simulating the pineapple express in the half degree community climate system model, ccs4, *Geophysical Research Letters*, 43(14), 7767–7773, doi:10.1002/2016GL069476.
- Shortridge, A., and J. Messina (2011), Spatial structure and landscape associations of SRTM error, *Remote Sensing of Environment*, 115(6), 1576–1587, doi:10.1016/j.rse.2011.02.017.

- Slangen, A., M. Carson, C. Katsman, R. Van de Wal, A. Köhl, L. Vermeersen, and D. Stammer (2014), Projecting twenty-first century regional sea-level changes, *Climatic Change*, 124(1-2), 317–332, doi:10.1007/s10584-014-1080-9.
- Sweet, W. V., R. E. Kopp, C. P. Weaver, J. Obeysekera, R. Horton, E. R. Thieler, and C. Zervas (2017), Global and regional sea level rise scenarios for the United States, *Technical Report NOS CO-OPS 083*, National Oceanic and Atmospheric Administration.
- Taylor, K. E., R. J. Stouffer, and G. A. Meehl (2012), An overview of CMIP5 and the experiment design, *Bulletin of the American Meteorological Society*, 93(4), 485–498, doi:10.1175/BAMS-D-11-00094.1.
- Wada, Y., L. P. H. van Beek, F. C. Sperna Weiland, B. F. Chao, Y.-H. Wu, and M. F. P. Bierkens (2012), Past and future contribution of global groundwater depletion to sea-level rise, *Geophysical Research Letters*, 39(9), L09,402, doi:10.1029/2012GL051230.
- Wong, T. E., A. M. R. Bakker, and K. Keller (2016), Impacts of Antarctic fast dynamics on sea-level projections and coastal flood defense, *ArXiv e-prints*, p. eprint arXiv:1612.07175.
- Wuebbles, D., D. Fahey, K. Hibbard, et al. (in review), Climate science special report, *Tech. rep.*, U.S. Global Change Research Program.
- Wuite, J., H. Rott, M. Hetzenecker, D. Floricioiu, J. De Rydt, G. Gudmundsson, T. Nagler, and M. Kern (2015), Evolution of surface velocities and ice discharge of larsen b outlet glaciers from 1995 to 2013, *The Cryosphere*, 9, 957–969, doi:10.5194/tc-9-957-2015.

Supporting Information for “Implications of ice-shelf hydrofracturing and ice-cliff collapse mechanisms for sea-level projections”

Robert E. Kopp¹, Robert M. DeConto², Daniel A. Bader³, Carling C. Hay^{1,4}, Radley M. Horton³, Scott Kulp⁵, Michael Oppenheimer⁶, David Pollard⁷, Benjamin H. Strauss⁵

¹Department of Earth & Planetary Sciences and Institute of Earth, Ocean & Atmospheric Sciences, Rutgers University, New Brunswick, NJ, USA

²Department of Geosciences, University of Massachusetts–Amherst, Amherst, MA, USA

³Center for Climate Systems Research, Columbia University, New York, NY, USA

⁴Department of Earth & Planetary Sciences, Harvard University, Cambridge, MA, USA

⁵Climate Central, Princeton, NJ, USA

⁶Woodrow Wilson School of Public & International Affairs and Department of Geosciences, Princeton University, Princeton, NJ, USA

⁷Earth and Environmental Systems Institute, Pennsylvania State University, University Park, PA, USA

Contents

1. Text S1
2. Data Set S1
3. Data Set S2
4. Data Set S3
5. Data Set S4
6. Data Set S5
7. Data Set S6

Text S1: Population Exposure Assessment Detailed Methods.

To assess topography as required for this analysis, we employ the NASA SRTM digital elevation model, which is based on a radar satellite mission in 2000. This Data Set has nearly global coverage (including latitudes 60N–54S, covering land inhabited by more than 99.9 percent of global population), and is available at a 1 arcsec (SRTM 3.0) horizontal resolution [NASA JPL, 2013]. SRTM, as distributed, is referenced to the EGM96 geoid (henceforth denoted by $SRTM_{EGM96}$) at a 1 m vertical resolution, with RMSE less than 10 m [LaLonde *et al.*, 2010; Rodriguez *et al.*, 2005]. Derived from radar measurements, $SRTM_{EGM96}$ is an unclassified (surface) elevation model, and significant positive bias is expected in regions of dense urban development and vegetation [Shortridge and Messina, 2011].

To convert elevations to a tidal vertical datum, we use the global mean sea level (MSL) model MSS_CNES_CLS_11 [AVISO, 2011], based on TOPEX/Poseidon satellite measurements, and referenced to the GLAS ellipsoid (MSL_{GLAS}). We also employ mean higher-high water ($MHHW_{MSL}$) deviations from MSL provided by Mark Merrifield, University of Hawaii, developed using the model TPX08 [Egbert and Erofeeva, 2002]. We convert MSL and SRTM to a common ellipsoidal datum (WGS84), and subtract the MHHW grids from MSL_{WGS84} to find $MHHW_{WGS84}$. We then subtract this tidal grid from $SRTM_{WGS84}$ to produce our final elevation map, $SRTM_{MHHW}$.

We resample a given relative sea-level rise projection grid X using bilinear interpolation to match the horizontal resolution of SRTM, and threshold elevation against these water heights to produce the inundation surface $THRESH_x$. Hydrological connectivity to the ocean is typically enforced in such analyses, but we find that high-frequency errors present in SRTM create significant speckle noise in the flood maps, causing some truly connected

areas to appear isolated. We instead perform connected components analysis at the 20m water height above MHHW, producing surface $CONTIG_{20m}$, and perform the intersection $HYBRID_x = THRESH_x \cap CONTIG_{20m}$. Isolated, low-lying land separated from ocean by at least a 20m high ridge is therefore removed from the final surface, $HYBRID_x$, while low-lying ocean-side land is included, reducing sensitivity to speckle noise. We compute inundation surfaces given different projection models (K14 and DP16), emissions scenarios (RCP 2.6 and RCP 8.5), percentiles of RSL projections (5th, 50th, and 95th), and years (2100 and 2300).

To assess population exposure, we employ the 2010 Landsat Data Set, which provides total estimated populations living in 1 km square cells [Bright *et al.*, 2011]. We refine this data using the SRTM Water Body Data Set (SWBD), which defines land cells at 1-arcsecond resolution. We resample Landsat at 1-arcsecond resolutions to align with the SRTM grids, assuming zero population in water cells, while proportionally increasing the population density in land cells to ensure total population in each 1 km square remains unchanged. We integrate exposure under each inundation surface and tabulate according to national boundaries defined by the Global Administrative Areas (GADM) 2.0 Data Set [Hijmans *et al.*, 2012].

Linked to the positive bias in SRTM elevation data, a notable negative bias has been detected in coastal population flood exposure analysis based on SRTM, at least within the United States, where higher quality, LIDAR-based elevation models are freely available for comparison [Kulp and Strauss, 2016]. LIDAR-based US national exposure estimates are ~45% higher than SRTM-based estimates at 1 m above MHHW; ~150% higher at 2 m and 3 m; and monotonically decline to ~33% higher at 10 m [Kulp and Strauss, 2016]. The exposure values presented here can thus be viewed as likely to significantly underestimate the true hazard. We nevertheless include them to provide some illustration of the ramifications of different projections. SRTM data are widely used in analysis of global exposure to sea level rise and coastal flooding [e.g., Hinkel *et al.*, 2014], and the major available alternative, the Global Land One-kilometer Base Elevation (GLOBE) gridded elevation model, is far coarser in resolution and based on underlying data of varying and unknown quality by region [Kulp and Strauss, 2016].

Data Set S1

Data Set S1 provides time series of WAIS, EAIS and total AIS contributions to GMSL from 2000 to 2300 from DP16.

Data Set S2

Data Set S2 provides estimated non-climatic background rates and IDs, latitude, and longitude of tide-gauge and grid point locations.

Data Set S3

Data Set S3 provides K14 GMSL and RSL projections at decadal intervals from 2010 to 2300.

Data Set S4

Data Set S4 provides DP16 GMSL and RSL projections at decadal intervals from 2010 to 2300.

Data Set S5

Data Set S5 provides DP16 GMSL and RSL projections at decadal intervals from 2010 to 2300 without bias correction.

Data Set S6

Data Set S6 provides population exposure by country in 2100 and 2300 under K14 and DP16 RSL projections.

Table S1. CMIP5 models used for thermal expansion and oceanographic processes

Model	Oceanographic			GIC		
	RCP 8.5	RCP 4.5	RCP 2.6	RCP 8.5	RCP 4.5	RCP 2.6
access1-0	21	21				
access1-3	21	21				
bcc-csm1-1	23	23	23	23	23	23
bcc-csm1-1-m	21	21	21			
canesm2	21	23	23	21	23	23
ccsm4	21	21	21	21	21	21
cmcc-cesm	21					
cmcc-cm	21	21				
cmcc-cms	21	21				
cnrm-cm5	23	23	21	23	23	21
csiro-mk3-6-0	21	21	21	23	23	21
gfdl-cm3	21	23	21	21	21	21
gfdl-esm2g	21	21	21			
gfdl-esm2m	21	21	21			
giss-e2-r	23	23	23	23	23	
giss-e2-r-cc	21	21				
hadgem2-cc	21					
hadgem2-es	21		23	23	23	23
inmcm4	21	21		21	21	
ipsl-cm5a-lr	23	23	23	23	23	23
ipsl-cm5a-mr	21	23	21			
miroc-esm	21	23	21	21	21	21
miroc-esm-chem	21	21	21			
miroc5				21	21	21
mpi-esm-lr	23	23	23	23	23	23
mpi-esm-mr	21	21	21			
mri-cgcm3	21		21	21	21	21
noresm1-m	21	23	21	21	23	21
noresm1-me	21	21	21			

21 = to 2100, 23 = to 2300.

Table S2. Projections of GMSL rise without bias correction (cm)

	50	17–83	5–95	1–99	99.9
RCP 8.5					
2050	26	20–33	16–39	12–45	51
2100	134	89–202	76–224	64–244	277
2200	713	579–892	530–959	495–1047	1193
2300	1169	981–1410	913–1553	861–1752	2007
RCP 4.5					
2050	22	16–28	12–33	9–38	42
2100	74	51–115	41–134	33–149	168
2200	241	134–386	104–439	79–489	571
2300	397	224–582	164–680	118–789	983
RCP 2.6					
2050	20	15–25	11–29	8–33	37
2100	44	31–62	23–75	15–87	101
2200	86	58–123	40–153	25–194	267
2300	109	66–172	39–238	16–336	492

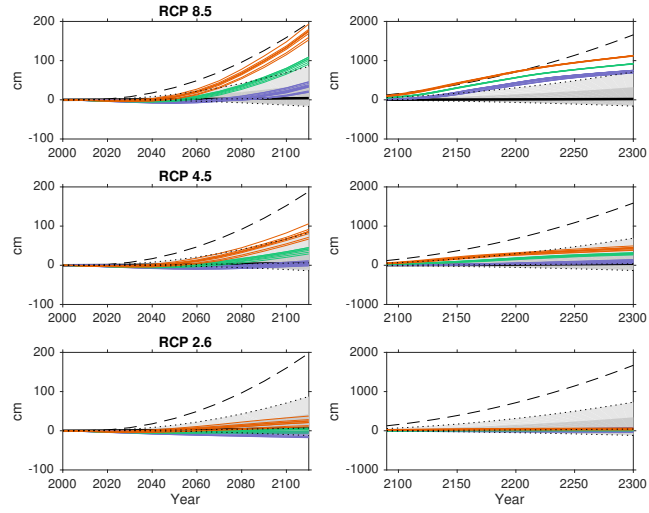


Figure S1. Antarctic ice sheet projections under the three RCPs without bias correction.

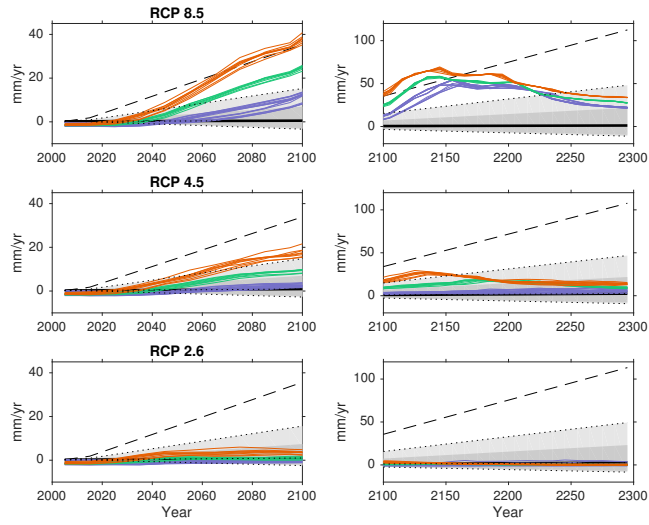


Figure S2. Rates of change of Antarctic ice sheet mass under the three RCPs without bias correction.

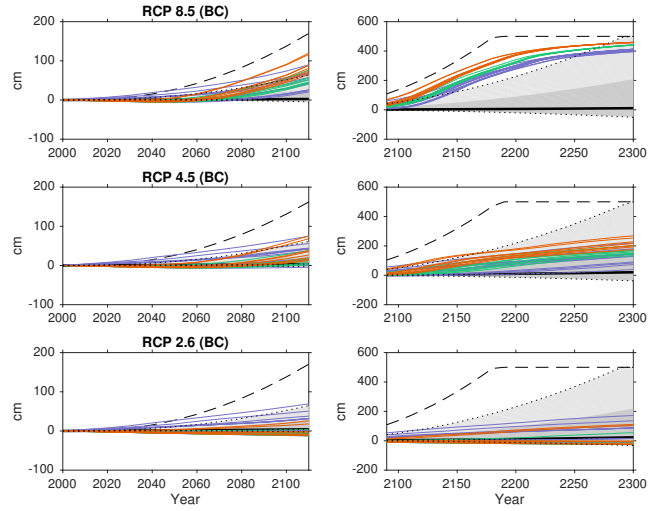


Figure S3. West Antarctic ice sheet projections under the three RCPs.

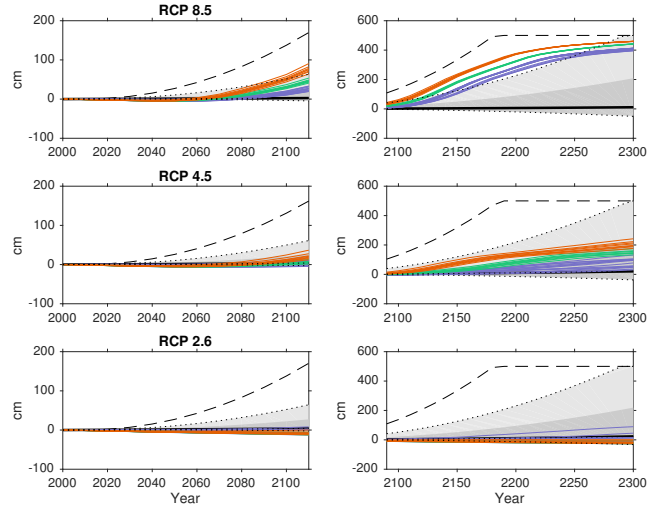


Figure S4. West Antarctic ice sheet projections under the three RCPs without bias correction.

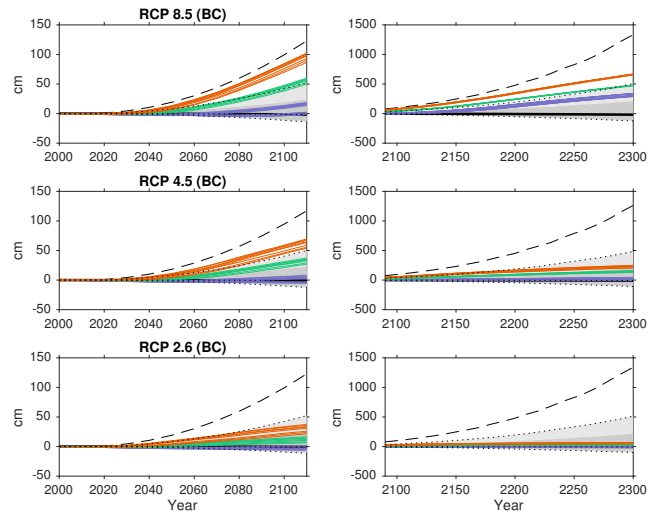


Figure S5. East Antarctic ice sheet projections under the three RCPs.

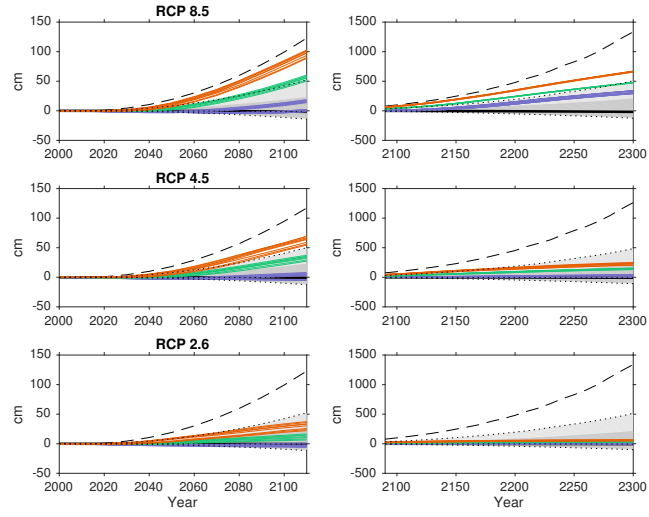


Figure S6. East Antarctic ice sheet projections under the three RCPs without bias correction.

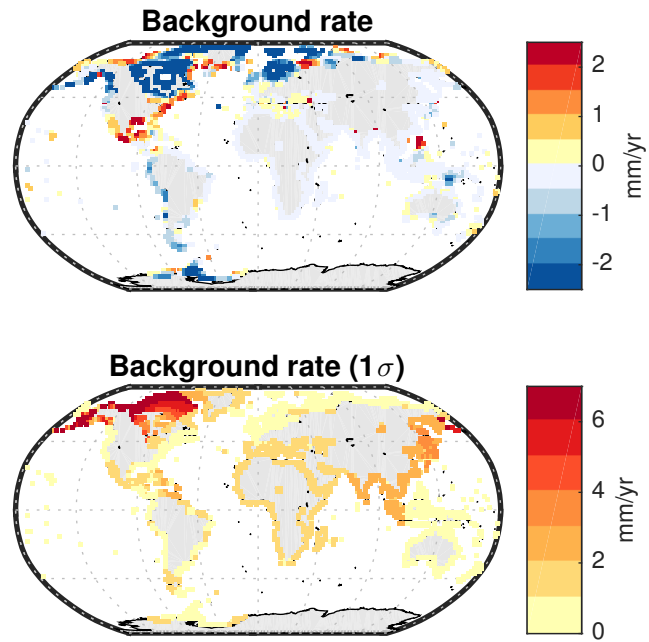


Figure S7. Non-climatic background rates estimated on a grid using the spatio-temporal statistical model of tide-gauge data. (a) Mean estimate, (b) standard deviation.

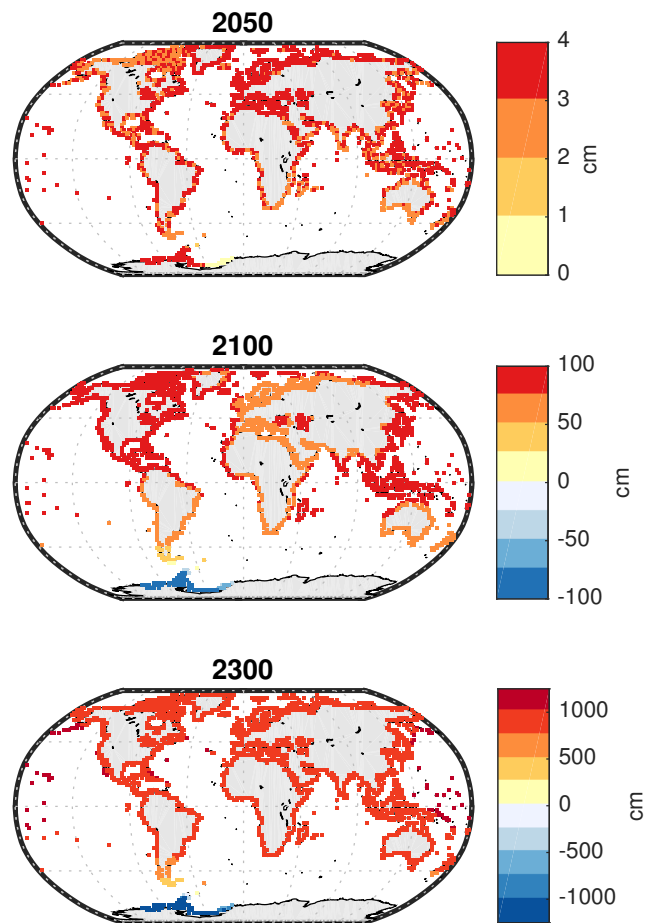


Figure S8. Difference in median RSL projections under RCP 8.5 in 2050, 2100 and 2300, relative to Kopp et al. (2014).

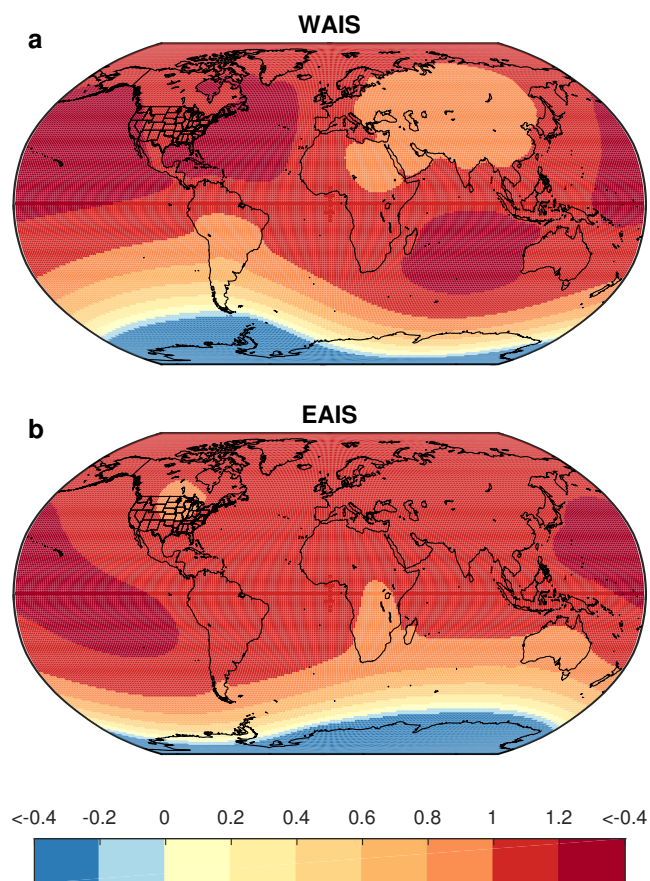


Figure S9. Static-equilibrium relative sea-level fingerprints of (a) the West Antarctic Ice Sheet and (b) the East Antarctic Ice Sheet, as used in this analysis. Units are ratio of relative sea-level change to global mean sea-level change.